1   **Title:** Dynamic triggering of creep events in the Salton Trough, Southern California by

2   regional M ≥ 5.4 earthquakes constrained by geodetic observations and numerical

3   simulations

4

5   **Authors**

6   Meng Wei, University of Rhode Island, Narragansett, RI, USA

7   Yajing Liu, McGill University, Montréal, Québec, Canada

8   Yoshihiro Kaneko, GNS Science, Lower Hutt, New Zealand

9   Jeffrey J. McGuire, Woods Hole Oceanographic Institution, Woods Hole, MA, USA

10   Roger Bilham, University of Colorado Boulder, Boulder, CO, USA

11

12   Corresponding author: M. Wei, Graduate School of Oceanography, University of Rhode

13   Island, Narragansett, RI 02882, U. S. A. (matt-wei@uri.edu)

14

15   Highlights

16   • We document fault creep on the Superstition Hills Fault (SHF) since 1988

17   • Many SHF creep events were dynamically triggered

18   • Shallow frictional heterogeneity explains both spontaneous and triggered creep

19   events

20   • Triggering depends on the peak amplitude of and the time-integrated dynamic

21   Coulomb stress

22   • The threshold for dynamic triggering of creep events on the SHF is about 0.6 MPa

23

Abstract

Since a regional earthquake in 1951, shallow creep events on strike-slip faults within the Salton Trough, Southern California have been triggered at least 10 times by M $\geq$ 5.4 earthquakes within 200 km. The high earthquake and creep activity and the long history of digital recording within the Salton Trough region provide a unique opportunity to study the mechanism of creep event triggering by nearby earthquakes. Here, we document the history of fault creep events on the Superstition Hills Fault based on data from creepmeters, InSAR, and field surveys since 1988. We focus on a subset of these creep events that were triggered by significant nearby earthquakes. We model these events by adding realistic static and dynamic perturbations to a theoretical fault model based on rate- and state-dependent friction. We find that the static stress changes from the causal earthquakes are less than 0.1 MPa and too small to instantaneously trigger creep events. In contrast, we can reproduce the characteristics of triggered slip with dynamic perturbations alone. The instantaneous triggering of creep events depends on the peak and the time-integrated amplitudes of the dynamic Coulomb stress change. Based on observations and simulations, the stress change amplitude required to trigger a creep event of 0.01 mm surface slip is about 0.6 MPa. This threshold is at least an order of magnitude larger than the reported triggering threshold of non-volcanic tremors (2-60 KPa) and earthquakes in geothermal fields (5 KPa) and near shale gas production sites (0.2-0.4 kPa), which may result from differences in effective normal stress, fault friction, the density of nucleation sites in these systems, or triggering mechanisms. We conclude that shallow frictional heterogeneity can explain both the spontaneous and dynamically triggered creep events on the Superstition Hills Fault.

47

48   Key words: dynamic triggering; creep events; shallow frictional heterogeneity; amplitude

49   threshold; Superstition Hills Fault

50

51   **Introduction**

52   Static stress changes associated with a large earthquake decrease with the distance from

53   the hypocenter much faster than do peak dynamic stress changes (Cotton and Coutant,

54   1997). Therefore it is usually assumed that dynamic perturbations are the main cause for

55   triggering earthquakes outside the aftershock zone (< ~2 fault lengths of the epicenter).

56   Within the aftershock zone, it is believed that both static and dynamic stresses can trigger

57   aftershocks, even though it is still debated which mechanism is more important and likely

58   to explain both instantaneous triggering and delayed triggering (Kilb et al., 2000; Freed,

59   2005; Richards-Dinger et al., 2010). The static stress changes associated with Coulomb

60   stress change $\Delta\sigma_f$ accompanying fault slip   ($\Delta\sigma_f = \Delta\tau + f\Delta\sigma$, where $\Delta\tau$ is the shear

61   stress change, f is the coefficient of friction, and $\Delta\sigma$ is the normal stress change) can

62   account for some aftershock activity (Stein, 1999). However, a large volume of literature

63   based on observations, numerical modeling, and lab experiments reveals that dynamic

64   triggering involves numerous contributory phenomena, such as mainshock magnitude,

65   proximity, amplitude spectra, peak ground motion, and mainshock focal mechanisms

66   (Gomberg et al., 1998; Perfettini et al., 2003a, b; Brodsky and Prejean, 2005; Johnson et

67   al., 2008). Moreover, in a recent review of the response to 260 M ≥ 7.0 shallow (depth <

68   50 km) mainshocks in 21 global regions with local seismograph networks, Parsons et al.

69   (2014) concluded that the aforementioned factors may not be the dominant ones for

70 dynamic triggering of earthquakes and rather, azimuth and polarization of surface waves

71 with respect to receiver faults may play more important roles.

72

73 Stress changes accompanying a large earthquake not only trigger other earthquakes but

74 also induce aseismic slip on strike-slip faults. A creep rate reduction on the southern

75 Hayward fault after the 1989 Loma Prieta earthquake is consistent with the reduction of

76 shear stress induced by the earthquake (Lienkaemper et al., 2001). The 1983 Coalinga

77 earthquake appeared to have affected the creep rate on the creeping section of the San

78 Andreas Fault near Parkfield in a similar manner (Simpson et al., 1988). Du et al. (2003)

79 calculated the static stress change due to nearby earthquakes in the Salton Trough,

80 Southern California. They found in 7 out of 10 cases static stress changes promoted

81 triggered slip. In a numerical simulation they applied sinusoidal waves to a single-degree-

82 of-freedom spring-slider system to study the effect of dynamic triggering on fault creep.

83 They showed that certain types of transient loads can trigger a creep event. However, the

84 dynamic stress perturbations introduced in their simulation are hypothetical sinusoidal

85 waves and their model does not have depth-dependent fault properties, and hence the

86 model results cannot be directly compared to natural fault slip observations.

87

88 Recent advances in observations and numerical simulations encourage us to revisit the

89 topic to improve our understanding of creep events triggering by nearby large

90 earthquakes. Wei et al. (2013) developed a numerical fault model that can explain

91 geodetic and geological observations of spontaneous creep events on strike-slip

92 faults. This model can be modified to simulate triggered creep events and compare them

93   with observations. In addition, large amounts of seismic, strain and fault creep data are

94   now available in the Salton Trough. We have a very good record of both the forcing

95   function (strain changes from which we may infer stress changes) and the response of the

96   fault, i.e. surface creep events with known amplitudes. The study of near surface

97   triggering of fault slip is thus more precisely constrained than the study of triggered

98   subsurface earthquakes or non-volcanic tremors, where the fault response occurs deep

99   within the earth and where the location and time history of slip is rarely well constrained

100   by geodetic data. In the absence of the time history of triggered slip the measured

101   response is usually a rate change that poorly constrains mechanical models.

102

103   In this paper, we focus on the causal mechanism of episodic creep events on the

104   Superstition Hills Fault (SHF) triggered by moderate earthquakes in and near the Salton

105   Trough. Prior to the November 24th, 1987, Mw 6.5 earthquake on the SHF, slip rates on

106   the fault were less than 0.5 mm/yr (Louie et al. 1985). After 1987, more than 25 years of

107   surface afterslip has been recorded (Bilham 1989; Rymer et al., 2002; Wei et al., 2011,

108   2013). To begin, we construct a comprehensive catalog of creep events on the SHF based

109   on data from geological surveys, creepmeter and Interferometric Synthetic Aperture

110   Radar (InSAR) measurements. Next, we constrain the static and dynamic perturbations

111   on SHF from six $M \geq 5.4$ earthquakes based on published papers and strong motion data,

112   respectively. Finally, realistic static and dynamic perturbations for the 1992 Mw 7.3

113   Landers, 1999 Mw 7.1 Hector Mine, and 2010 Mw 7.2 El Mayor were analyzed using the

114   numerical fault model proposed by Wei et al. (2013).

115

Observations of creep events at Salton Trough, Southern California

On many creeping faults, surface creep consists of continuous creep and episodic creep events (Bilham, 1989; Wei et al., 2013). Creep events occur spontaneously, or during the passage of surface waves from nearby earthquakes (Rymer et al., 2002), or in response to soil moisture changes (Schulz et al., 1983). The Salton Trough is a sedimentary basin at the southern end of the San Andreas Fault system near the US and Mexico border. Records of triggered slip are available for more than ten occasions from the Superstition Hills Fault (SHF), the San Andreas Fault, and the Imperial Fault as well as from numerous minor faults in the Coachella and Imperial Valleys (Rymer et al., 2002; Wei et al., 2011, 2013). Since 1950, more than 10 earthquakes with M ≥ 5.4 have occurred within 200 km from this region (Figure 1), many of which triggered creep events on multiple faults (Table S1 in the supplementary material). From Table S1 it is evident that triggered surface slip can occur when the host fault lies within 150 km of a Mw>7 earthquake, within 80 km of a Mw>6 earthquake, or within 20 km of a Mw>5 earthquake. Not all triggered slip occurs on faults recognized to be actively creeping, but in general those that exhibit steady slow surface creep or episodic creep events are regularly triggered by nearby earthquakes.

The SHF has over 60 years of record of triggered creep as early as 1951 (Allen et al., 1972) and over 25 years of digital data. Since 1951, creep events on the SHF were triggered by the 1968 Mw 6.5 Borrego Mountain, 1979 Mw 6.4 Imperial, 1981 Mw 5.8 Westmoreland, 1992 Mw 7.3 Landers, 1999 Mw 7.1 Hector Mine, 2010 Mw 7.2 El

139   Mayor (Rymer et al., 2002; Wei et al., 2011 and references therein), and the 2012 Mw 5.4

140   Brawley (Hauksson et al., 2013) earthquakes. The largest observed triggered creep event

141   has a surface slip of 22 mm and the smallest of 0.17 mm (Table 1). Determining the exact

142   timing and associated uncertainties of triggered creep depends on available

143   measurements. For the seven earthquakes mentioned above, creepmeter measurements

144   are available only for creep events triggered by the 1992 Landers and Big Bear

145   earthquakes, the 2010 El Mayor and the 2012 Brawley earthquakes. Where data with a

146   sample rate of 1 minute were available in 1992 it appears that triggered slip accompanies

147   the passage of surface waves (Bodin et al, 1994). The timing of creep associated with

148   other earthquakes relies on field survey and InSAR, and therefore we can only confirm

149   that creep occurred within 24 hours after the mainshock.

150

151   The history of SHF creep events is complementarily constrained by geological surveys,

152   creepmeter and InSAR measurements. Field survey on the SHF has been conducted since

153   1950s after each regional large earthquake (Rymer et al., 2002). An analogue creepmeter

154   was installed on the SHF in 1967 by Caltech but it recorded negligible creep (Louie et al.,

155   1985). Three digital creepmeters operated on the SHF for five years following the 1987

156   Mw 6.6 SHF earthquake (Bilham et al., 2004). Recording was resumed with a single

157   creepmeter in March 2004. The sampling rate of a creepmeter is typically 1-5 minutes

158   (Bilham et al., 2004). InSAR data became available following the launch of the ERS

159   satellite in 1992, and the interval between ERS/Envisat InSAR observations is 35 days.

160   Field surveys usually occur within 24 hours of the mainshock (Rymer et al., 2002).

161

162 **Table 1**. Triggered slip amplitude on SHF by major regional earthquakes
163

Year	M_w	Earthquake	Static perturbations* (MPa)	Dynamic perturbations**		SHF	
				Maximum and minimum dynamic Coulomb stress (MPa)		Maximum slip on SHF (cm)	Distance from earthquake (km)
1968	6.5	Borrego Mountain	0.03[1]	N/A		2.5	40
1979	6.4	Imperial	0.03[1]	0.8 (-0.7)		2.0	45
1981	5.8	Westmorland	0.05[1]	2.9 (-2.4)		1.4	20
1986	6.0	North Palm Springs	<0.0001[1]	N/A		N/A	139
1992	7.3	Landers	<0.0001[1,2,3]	0.5 (-0.6)		2.5	155
1994	6.7	Northridge	<0.0001[1]	N/A		N/A	295
1999	7.1	Hector Mine	<0.0001[3]	0.5 (-0.5)		2.0	190
2010	7.2	El Mayor-Cucapah	-0.02[5]	1.6 (-1.6)		2.7	85
2012	5.4	Brawley	0.07[4]	0.05 (-0.05)		0.014	15

164
165 * The main sources: 1: *Du et al.*, 2004; 2: *King et al.*, 1994; 3: *Fialko et al.*, 2002; 4: *Hauksson et al.,* 2013;
166 5: *Toda and Stein*, http://supersites.earthobservations.org/Baja_stress.png.
167
168 ** Based on the closest strong motion station. Data were downloaded from http://strongmotioncenter.org/,
169 rotated to normal and shear directions on the SHF, and translated, respectively, to normal and shear stresses
170 by following $\tau = \frac{dD}{dt}/V_g * \mu$, where D is the strong motion data in displacement, V_g is the surface wave's
171 group velocity (3.5 km/s), and μ is the shear modulus (30 GPa).
172

173 Aiming to find possible creep events during the 1992-2004 time period when the

174 creepmeter was off-line, we analyzed ERS InSAR images (Track 356 Frame 2943, Figure

175 2). The data were downloaded from the UNAVCO SAR archive and processed with

176 GMTSAR (http://topex.ucsd.edu/gmtsar/). Based on the InSAR data, we infer that at least

177 two previously unknown large events occurred between 1993-1996. Assuming most of

178 the deformation is horizontal (there is no topographic step across the fault) we estimated

179 a displacement of 1-2 centimeter for both events (Figure 2). Robert Sharp (personal

180 communication, 1999) observed one of these 2 cm events in the field but its time is not

181   well resolved. The first event occurred between 11/03/1993 to 07/13/1995, and the

182   second one occurred between 10/11/1996 and 12/20/1996. The timing of the second

183   event is better constrained than the first event because more SAR images became

184   available after the launch of ERS2 in 1995. Considering the magnitude and time range of

185   these two creep events, it is likely that each episode was a single event, although, due to

186   the InSAR time resolution, we cannot rule out the possibility that each consisted of

187   multiple smaller events. Figure 3 thus presents the most complete slip history of creep

188   events on a strike-slip fault up to date. We also found two creep events that only slipped

189   at the northern segment of SHF. We do not include them in the creep time series in

190   Figure 3 because the creepmeter is located in the southern segment of SHF. Many creep

191   events occurred during 1988-1991 but there was only one case in that time period where

192   a M4.7 likely triggered slip on SHF (Williams and Magistrale, 1989). Part of this is due

193   to the paucity of M>4 aftershocks (Bilham 1989). There were only three M>4 aftershocks

194   since the installation of the creepmeters in December 1987, and the last one occurred in

195   March 1988. Since then, there was no M>4 earthquake on the SHF.

196

197
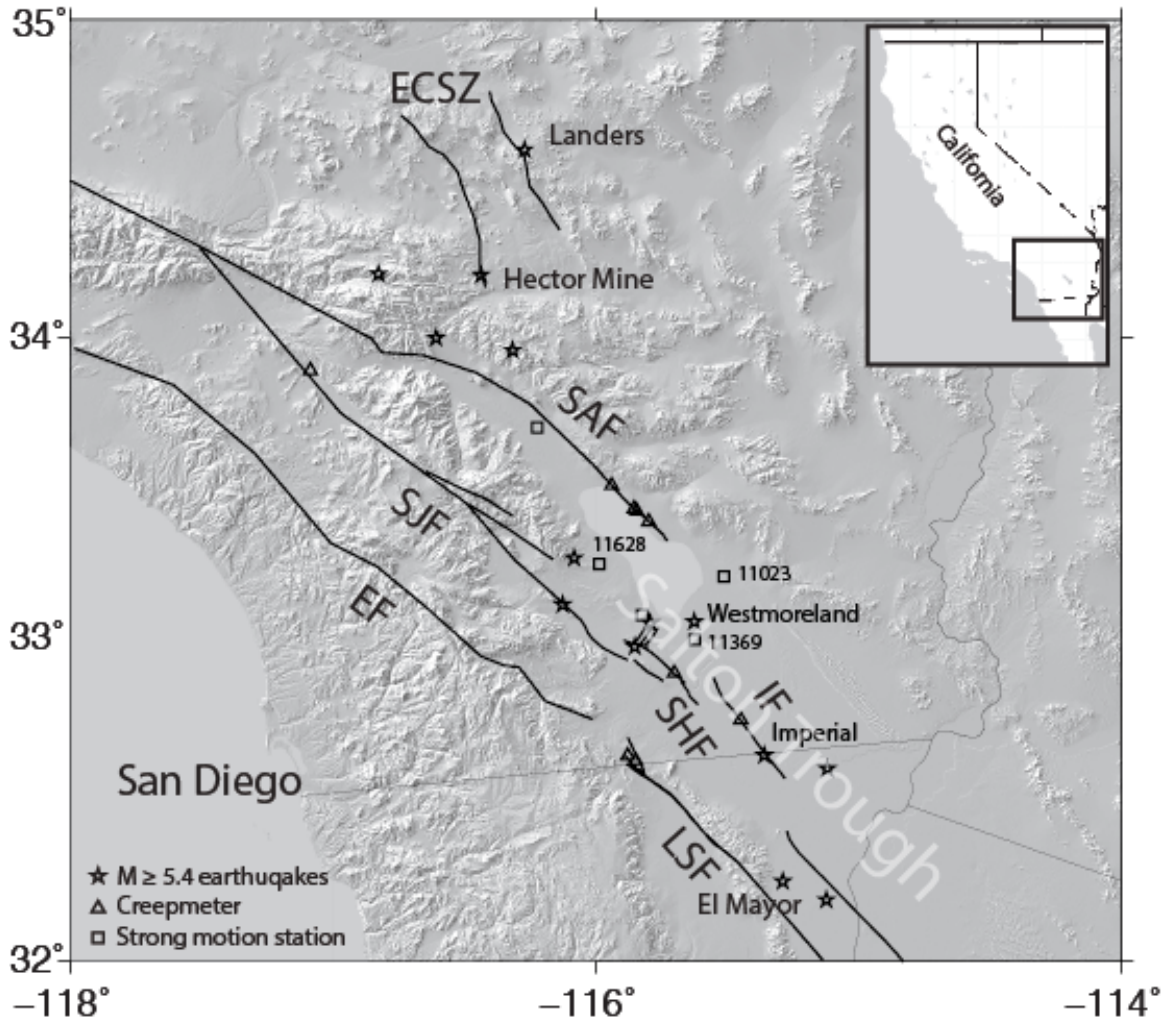
Figure 1. Study area in Southern California. The Salton Trough is the region of low relief in the SE corner of the map. Stars show moderate (M≥5.4) earthquake epicenters with significant events labeled. Triangles are locations of creepmeters. Open squares show nearby strong motion stations (station number indicated). Fault names are abbreviated as following: Eastern California Shear Zone (ECSZ), San Andreas Fault (SAF), San Jacinto fault (SJF), Elsinore fault (EF), Superstition Hills fault (SHF), Imperial fault (IF), and Laguna Salada fault (LSF).
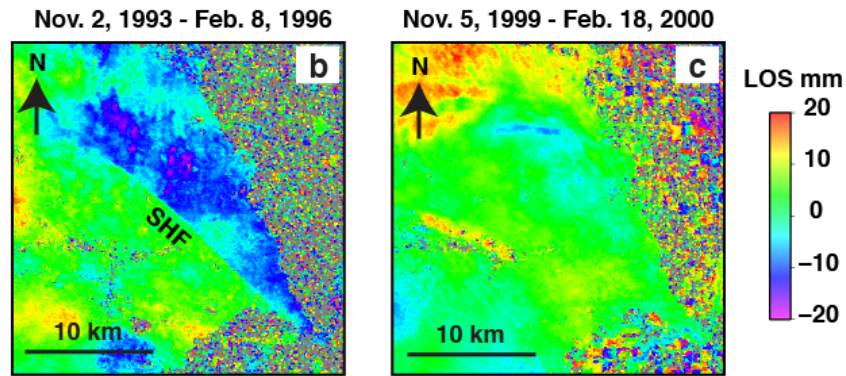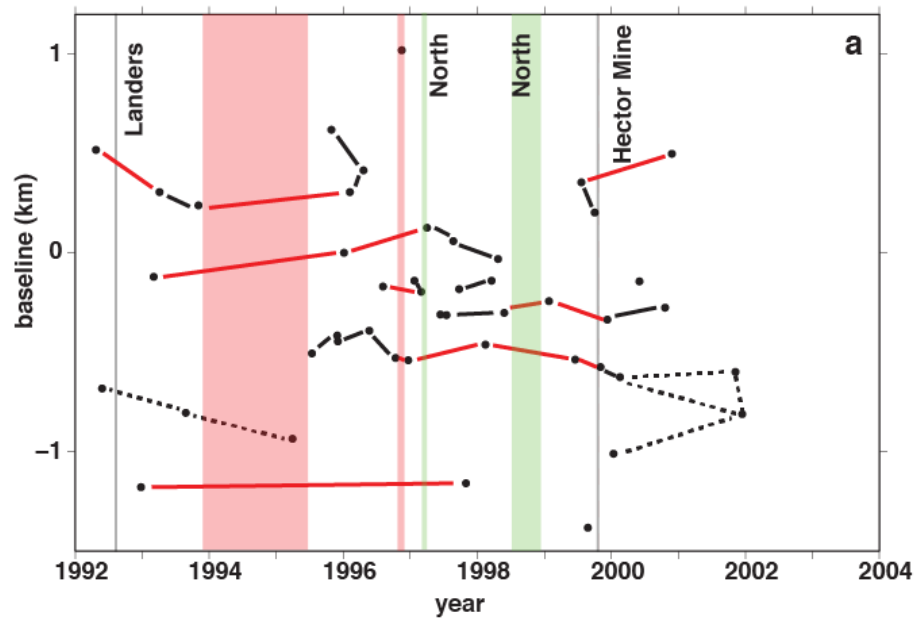
Figure 2. InSAR data used to identify creep events on the SHF. (a) Time-baseline map of InSAR data used in this study. A baseline is the distance between the satellite positions when the SAR images were acquired. A short baseline (< ~250 m) is required to make interferograms. Red and black solid lines link the pairs that show or lack displacement on the SHF (phase change across the fault trace) respectively. Dashed black lines denote pairs with interferrograms that were too noisy to determine fault motion. Pink rectangles highlight the possible time periods for the two newly identified creep events. Green rectangles highlight two events that slipped only at the northern segment of the SHF. (b) Example InSAR image showing slip on the SHF as indicated by

217   the sharp boundary between the green region in the southwest and blue region in the northeast.

218   The phase change across the SHF is caused by displacement on the fault. The cloudy blue area is

219   likely water vapor noise. (c) Example InSAR image showing no slip on the SHF. The cloudy red

220   area in the top-left corner is also water vapor noise.

221
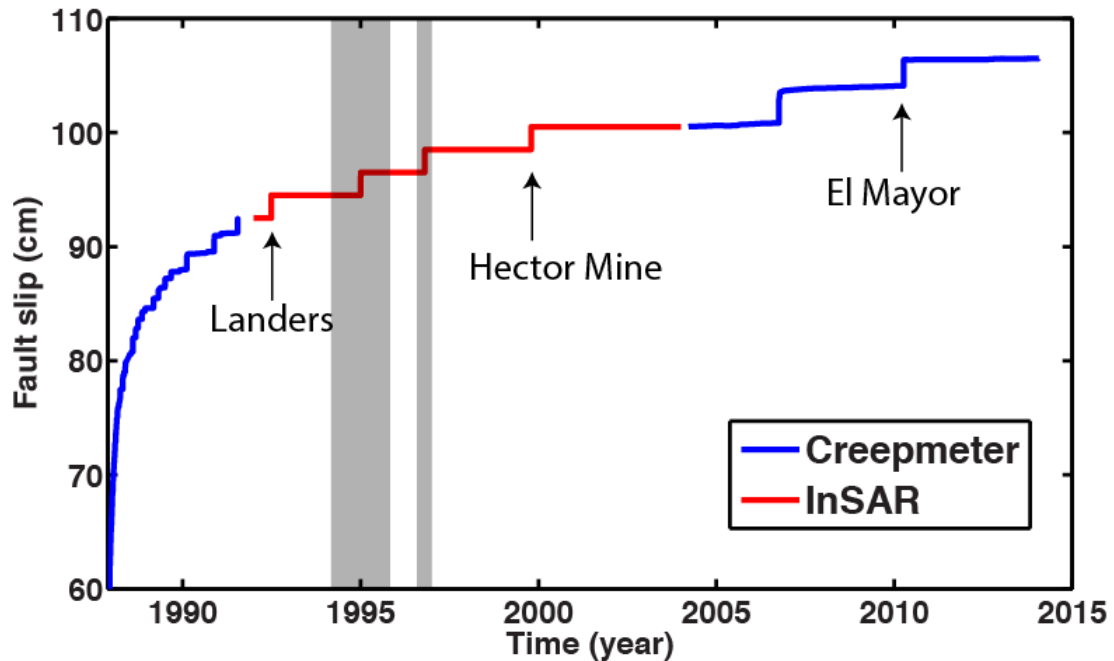
222

223   **Figure 3.** Composite afterslip history on the Superstition Hills Fault at the location of the Imler

224   Road creepmeter since 6 days after the 1987 M6.6 SHF mainshock, based on creepmeter and

225   InSAR data as well as field surveys. Field surveys provided ground-truth data for many creep

226   events. The absolute amplitude of fault slip at the starting point of each time series is unknown.

227   We aligned the three time series to form a continuous history. Gray bars show the range of

228   possible occurrence times of the two newly identified creep events as constrained by InSAR data.

229   Arrows point to creep events triggered by nearby large earthquakes.

230

231   **Observations and modeling of stress perturbations on the SHF**

12

232   The static Coulomb stress changes on the SHF produced by nearby large earthquakes

233   (Table 1 and references in the caption) are usually quite small (< 0.1 MPa). Du et al.

234   (2003) calculated the static Coulomb stress perturbations on the SHF to be less than 0.1

235   MPa for all major earthquakes before 1993. The static Coulomb stress change on the SHF

236   generated by the 1992 Landers and 1999 Hector Mine earthquakes were less than 1 kPa

237   (Fialko et al., 2002). For the 2010 Mw 7.2 El Mayor earthquake, the Coulomb stress

238   change on the SHF is negative (-0.02 MPa) and therefore acts to inhibit creep events

239   rather   than   triggering   them   (Toda   and   Stein,

240   http://supersites.earthobservations.org/Baja_stress.png). For the 1968 Mw 6.5 Borrego

241   Mountain, 1979 Mw 6.4 Imperial, 1981 Mw 5.8 Westmorland, the 2012 Mw 5.4 Brawley

242   earthquakes, both static and dynamic stress perturbations seemed to have promoted creep

243   events. The static Coulomb stress change at the southern segment of SHF is about 0.03,

244   0.03, 0.05 and 0.07 MPa, respectively (see references in Table 1). However, these

245   numbers are 1-2 orders of magnitude smaller than the dynamic stress perturbations with

246   the exception of the 2012 Mw 5.4 Brawley earthquake, which is very close to SHF. We

247   will later show that these static stress changes are too small to trigger creep events.

248   Instead, dynamic perturbations are the main mechanism of triggering creep events at

249   SHF.

250

251   The dynamic stress changes were constrained mainly by strong motion data, which are

252   available for many of the relevant events over the last 40 years. A potential instrumental

253   problem with strong motion sensors is that they are not designed to accurately record

254   long period (> 10s) seismic waves (Boore and Bommer, 2005). With the notion that

255   longer period perturbations might be the most important in triggering (Brodsky and

256   Prejean, 2005), we used high-rate GPS data (Bock et al., 2011) to validate the use of

257   strong motion data alone for computing dynamic stress perturbations in this region. The

258   comparison between high-rate GPS (1 Hz) and strong motion and combined GPS-strong-

259   motion shows that the strong motion sensor records very likely reflect the true ground

260   motion for nearby large earthquakes in this region (Figure S1 in the supplementary

261   material). For consistency, we use strong motion data to constrain the dynamic

262   perturbations even when high-rate GPS data are available for recent events. We primarily

263   rely on the strong motion station 11628 (30 km north of the northern end of SHF)

264   because it is the longest running (since at least 1992) and the closest station to SHF

265   (Figure 1). The strong motion displacement time series are rotated to the normal and

266   shear directions relative to the SHF fault plane, and translated respectively to normal and

267   shear stress changes using the equation: $stress = \frac{dD}{dt} * \mu/V_g$, where D is the strong

268   motion data in displacement, V_g is the group wave velocity (3.5 km/s), and μ is the shear

269   modulus (30 GPa). This assumes that large amplitude surface waves are more important

270   in triggering than body waves and that the surface waves can be treated as a plane wave

271   with a constant velocity. All the earthquakes listed in Table 1 show a peak-to-trough

272   amplitude of 0.5-1 MPa in dynamic perturbations at the Imler road site on the SHF and

273   are at least an order of magnitude larger than static stress changes, with the exception of

274   the 2012 Mw 5.4 Brawley earthquake, for which the static stress is as large as the

275   dynamic stress perturbation.

276

277   **Fault slip modeling in the framework of rate-and-state friction**

278 We next model the SHF as a 1D strike-slip fault with depth-variable frictional properties

279 in a 2D medium in the framework of laboratory-derived rate-and-state friction laws

280 (Dieterich, 1979; Ruina, 1983). Wei et al. (2013) proposed a model that includes three

281 layers of alternating frictional stability above the seismogenic zone (Figure 4) because the

282 traditional 3-layer model (Scholz, 1998) cannot simultaneously reproduce the continuous

283 afterslip and the episodic creep events observed following the 1987 Mw 6.6 SHF

284 earthquake. Specifically, a thin velocity-weakening (VW) layer is embedded within the

285 top stable zone. As a result, creep events nucleate in this small VW layer and propagate

286 to the surface, whereas long-term afterslip arises from the velocity-strengthening (VS)

287 layer beneath it. The continuous creep between successive creep events is due to the

288 existence of the top VS layer. The shallow VS layer might correspond to a special layer

289 observed in sediments in nearby drilling samples (Wei et al., 2013). Detailed studies

290 including well log data in the nearby Salton Sea Geothermal Field found that Salton

291 Trough sediments can switch from failing in creep events to rupturing in earthquakes

292 over just a few km due to hydrothermal alteration and the introduction of a significant

293 amount of feldsphar minerals (McGuire et al., 2015). Similar compositional

294 heterogeneity is possible at the SHF. This fault model can reproduce the geodetic and

295 geological observations, including coseismic slip, rapid afterslip, and spontaneous

296 episodic or continuous creep on the SHF (red line in Figure 5b; see Wei et al., 2013).

297 Following an earthquake, the rate of displacement contributed by successive creep events

298 decreases continuously, while the interval between events increases before reaching a

299 steady value, consistent with observations. The key parameters in the rate-and-state

300 friction model include a, b, D_c, and $\bar{\sigma}$, where a and b are non-dimensional friction

301   stability parameters, D_c is the critical distance (sliding distance required to renew the

302   contact population on the fault following a velocity step), and $\bar{\sigma}$ is the effective normal

303   stress (normal stress minus pore pressure) (Dieterich, 1979; Ruina, 1983). In the shallow

304   VW layer (0.2-1 km depth) (Figure 4) we set: a-b = -0.004; a = 0.015; D_c = 0.2-0.7 mm;

305     $\bar{\sigma}$ = 5.6-15.6 MPa. The effective normal stress increases linearly with depth at a rate of

306   13 MPa/km (lithostatic minus hydrostatic) and a base value of 2.96 MPa at surface is

307   included.

308

309   Normal and shear stress perturbations (static or dynamic) can be applied on the fault at

310   any desired time in the simulated earthquake cycle. For the static cases, we apply the

311   stress change over the entire fault. For the dynamic cases, we apply the perturbations only

312   in the top 3 km where the largest surface wave amplitudes are expected. Fault slip rate

313   and state variable evolution following a stress perturbation are formulated based on

314   laboratory experiments (Linker and Dieterich, 1992; Richardson and Marone, 1999) and

315   are incorporated into the rate-and-state friction model as:

$$\frac{\theta_2}{\theta_1} = \left(\frac{\bar{\sigma}_1}{\bar{\sigma}_2}\right)^{\alpha/b} \tag{1}$$

$$\frac{V_2}{V_1} = \left(\frac{\bar{\sigma}_2}{\bar{\sigma}_1}\right)^{\alpha/a} exp\left(\frac{\tau_2}{a\bar{\sigma}_2} - \frac{\tau_1}{a\bar{\sigma}_1}\right) \tag{2}$$

318   where θ is the state variable and V is the slip rate. $\bar{\sigma}_1$ and $\bar{\sigma}_2$ are the effective normal

319   stress, and τ_1 and τ_2 are the shear stress, before and after the perturbation, respectively. α

320   is set to be 0.2 for a base friction of 0.6, measured by Linker and Dieterich (1994) and

321   Richardson and Marone (1999) on granite surface with gouge.
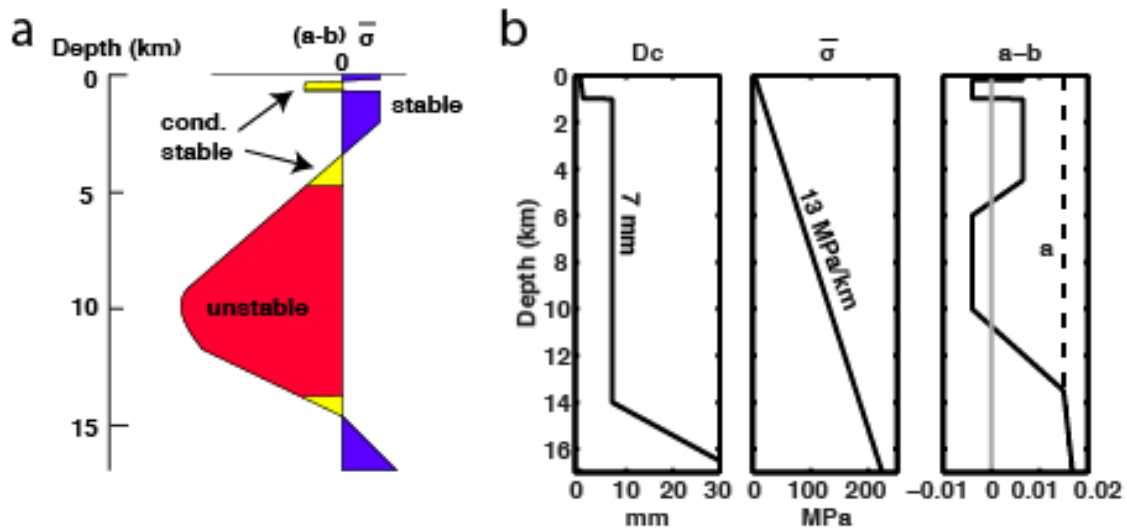
Figure 4. Physical parameters used in the fault model. (a) Schematic fault model. The yellow, blue, and red regions have conditionally stable, stable, and unstable frictional parameters respectively. (b) Variation of critical distance Dc, effective normal stress $\bar{\sigma}$, friction parameters a-b and a with depth. In the panel titled a-b, the black solid line shows the value of a-b, the dashed line shows the value of a, and the gray line shows a-b = 0 to illustrate the changes in frictional stability with depth.

329
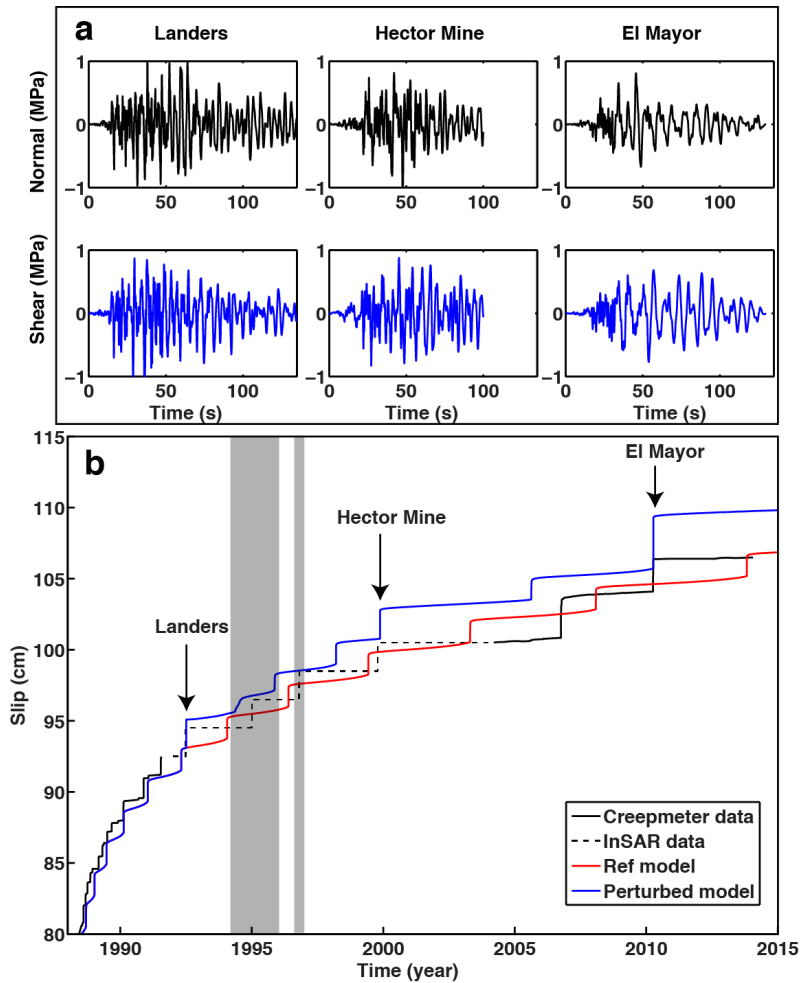
Figure 5. Numerical simulations and observed surface slip history on the SHF between 1988 and 2015. (a) Dynamic stress perturbations used to produce results in the perturbed model, which are applied at the times of the Landers, Hector Mine, and El Mayor earthquakes. These perturbations are scaled by a factor of 2.13, 2.023, and 0.538 from the stress perturbations derived from the strong motion data at stations 11628, 11628, and 11369, respectively. (b) The red solid line is the reference model with no perturbations added (Wei et al., 2013). The blue line shows a simulation that included all three perturbations.

337

338

339

340   Building upon the reference model as shown in Figure 5b (red solid line), we first added

341   static stress changes up to 0.1 MPa and found that these changes are too small to

342   instantaneously trigger creep events (< 0.01 mm slip within 24 hours). Then, we applied

343   dynamic perturbations of both normal and shear components, which are constrained by

344   strong motion data from the Landers, Hector Mine, and El Mayor earthquakes (Figure

345   5a). As shown in Figure 5b, the perturbed model (blue solid line) reproduces the observed

346   triggered slip of similar timing and displacement. This indicates that creep events on the

347   SHF are dynamically triggered by these three earthquakes. In addition, there seems to be

348   distinct temporal features between spontaneous and triggered creep events. A

349   spontaneous event includes slip acceleration over a few minutes followed by gradual

350   return to background slip rate over several hours or days, often including multiple small

351   creep events, whereas a triggered event is usually manifested as a single abrupt fault

352   displacement between two data samples (1-5 minutes). Our model reproduces this feature

353   of the creepmeter data (Figure 6). The reason for the difference is that when the top VS

354   layer is triggered by the transient dynamic perturbations very little energy is left for

355   afterslip between creep events. Our simulations also show that the same equivalent

356   Coulomb stress change, due to either shear stress only ($\Delta\sigma=0$) or normal stress only

357   ($\Delta\tau=0$), would trigger similar creep (Figure S2 in supplementary materials). This shows

358   that Coulomb stress change is a good indicator for triggering, as was suggested by

359   Perfettini et al. (2003b). In our model, we use a base friction of 0.6 to calculate the

360   Coulomb stress change.

361

362

363
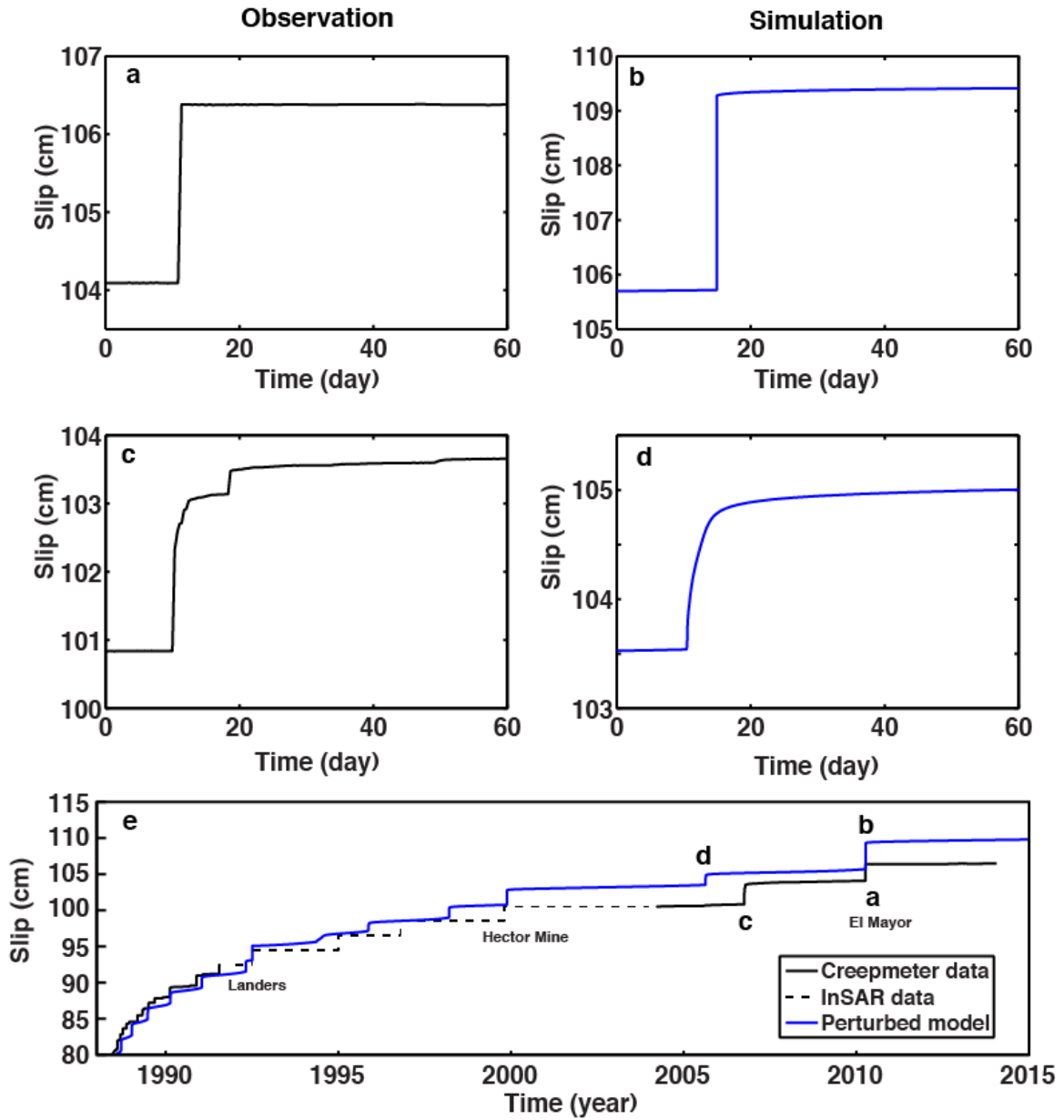
Figure 6. Creepmeter observations of the triggered event in 2010 (a), and the spontaneous event in 2006 (c), as well as our simulations of the triggered (b), and spontaneous (d) events. (e) Data and simulation, same as Figure 5b but the reference model (red line in Figure 5b) is not shown. This figure shows that our model can reproduce the distinct temporal features of both spontaneous and triggered creep events.

369

370

371 The displacement of triggered creep events scales with the maximum dynamic Coulomb

372 stress change (Figure 7a). To reproduce the proper displacement for each event, we have

373 to fine-tune the perturbations by applying appropriate scaling factors to the dynamic

374 perturbations derived from strong motion data. Such scaling factors would account for

375 the uncertainties in the calculation of dynamic stress perturbations from strong motion

376 observations, which are not situated directly on the fault, as well as for the uncertainties

377 in the parameters in our rate-and-state model. The modeled displacement scales

378 exponentially with the perturbations until it reaches a threshold, above which the slip

379 scales steeply and linearly with the perturbation and the triggered event becomes an

380 earthquake (maximum velocity > 10 cm/s) (Figure 7a). Thus, if a perturbation is

381 sufficiently strong, the event in the shallow VW layer will become seismic (Kaneko and

382 Lapusta, 2008). The slope of these scaling curves depends on the timing of perturbation.

383 For example, the slope for the Landers case is gentle because the perturbation occurs

384 during an early stage of the creep event cycle. In contrast, the slope for El Mayor is very

385 sharp because the shallow VW layer is close to failure when perturbation is introduced.

386 However, observations show no evidence of triggered earthquakes on SHF from these

387 three mainshock events. Either the perturbation was insufficient to trigger earthquakes or

388 our fault model is missing some physics such as dilatancy strengthening that can stabilize

389 slip (Segall et al., 2010; Liu, 2013) so that the triggered slip will not grow to earthquakes

390 even at very large perturbations.

391
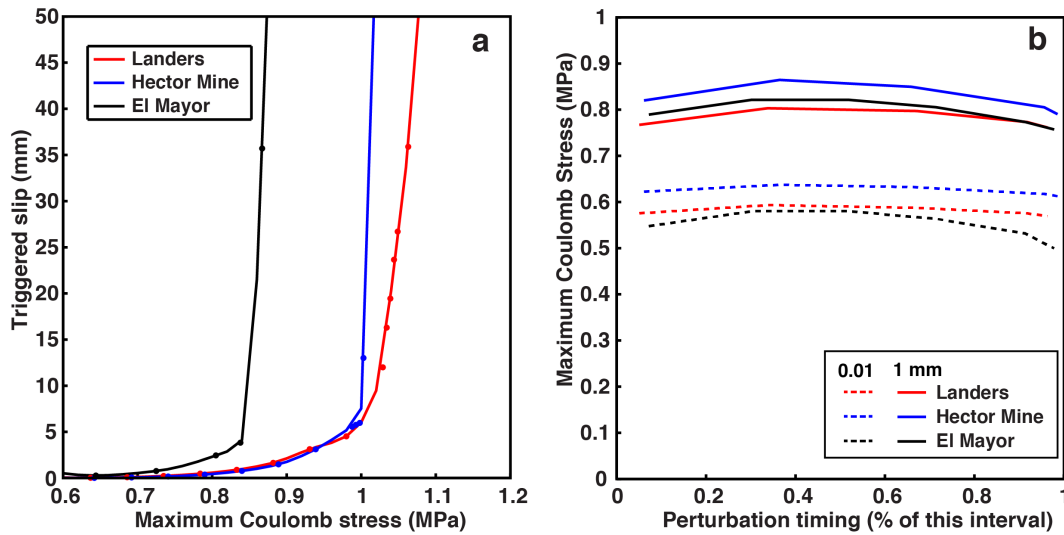
Figure 7. (a) Relation between the maximum dynamic Coulomb stress change and the amplitude
of triggered slip. For each earthquake, we use a perturbation derived from the strong motion
station as the reference perturbation. Then we scale the waveform with a range of factors as a
group of perturbations to understand the scaling. (b) Coulomb stress threshold for triggering 0.01
mm (dashed lines) and 1 mm (solid lines) of slip events as a function of time during an interval
between two successive creep events in our models. For each triggering earthquake, the timing of
the perturbation is varied within this interval.

399

Based on both observations and numerical simulations we may establish the perturbation
threshold needed to trigger creep events on the SHF. Observations (Table S1 in the
supplementary materials) show that triggering of creep events on the SHF requires a
Mw>7 within 150 km, Mw>6 within 80 km, and Mw>5 within 20 km. Earthquakes that
do trigger creep events on the SHF usually show a peak-to-trough amplitude of 0.5 - 1
MPa of the dynamic Coulomb stress change, whereas the earthquakes that do not trigger
creep events usually have a perturbation less than ~ 0.01 MPa on the SHF. This brackets
the triggering threshold to be somewhere between 0.01-1 MPa. With numerical

408   simulation, we can reduce this triggering threshold uncertainty. Taking the three

409   waveforms in Figures 5a as examples, we vary the timing of perturbation and scale the

410   waveforms to further constrain the triggering threshold. Because the resolution of the

411   Superstition Hills creepmeter is 9.6 μm during inter-seismic period and 1 mm during co-

412   seismic rupture (Bilham et al., 2004), we plot the stress threshold as a function of time

413   between two spontaneous creep events when the perturbation is introduced for the two

414   resolutions. The triggering threshold for 0.01 mm slip is about 0.6 MPa and the triggering

415   threshold for 1 mm slip is about 0.8 MPa (Figure 7b). Variation of the threshold with

416   time is small, with the maximum reached around the middle of the interval when the

417   shallow velocity-weakening layer has returned to a more firmly locked state.

418

419   In Figure 8 we present examples of modeling results for dynamic Coulomb stress

420   histories derived from the Landers earthquake data during the perturbation. We find the

421   triggered creep event usually consists of several individual events, each lasting less than 1

422   second (blue lines in Figure 8). The magnitude and timing of each individual event

423   depends on the dynamic Coulomb stress change. Noticeable slip will occur when the

424   Coulomb stress exceeds a threshold, 0.75 MPa for this case, and the displacement

425   depends on the amplitude of the stress above the threshold. Perturbations below this

426   threshold will not trigger any noticeable slip at this scale (red lines in Figure 8).

427   However, a Coulomb stress change above 0.6 MPa but below 0.75 MPa could trigger

428   small slip at a level of 0.01 mm, which is not visible at the scale presented in Figure 8c.

429
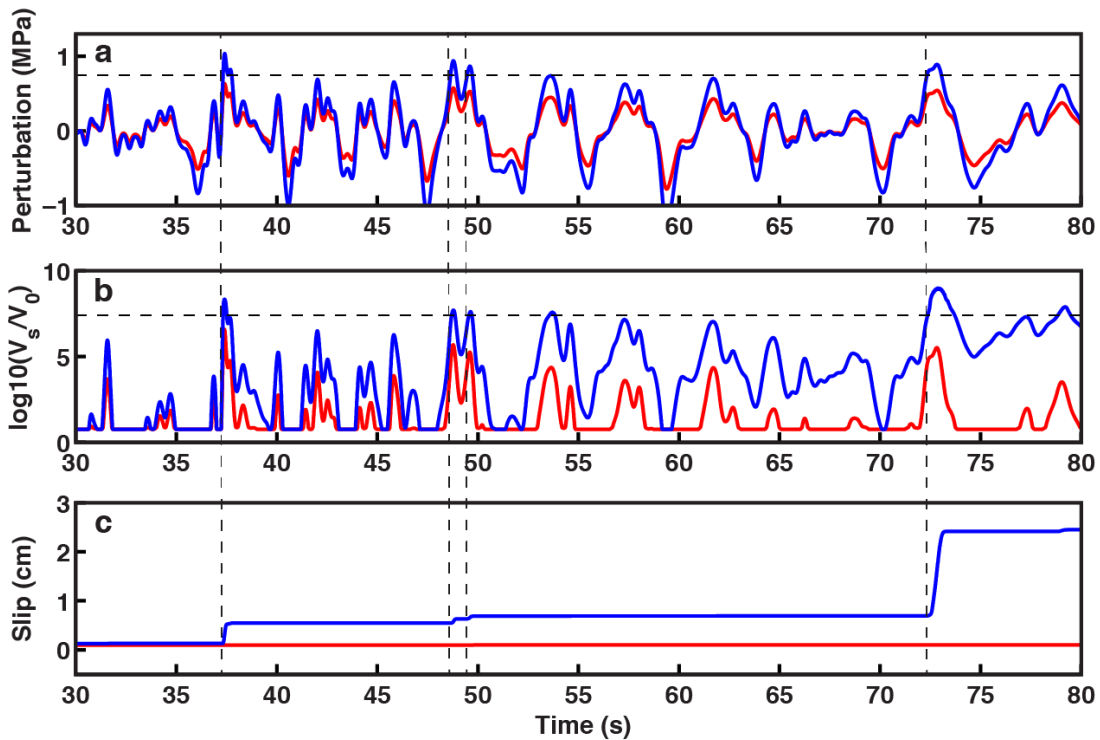
Figure 8. Effect of Coulomb stress change on the dynamic triggering of modeled creep events during the perturbation. (a) Coulomb stress perturbations applied in cases 1 and 2. Perturbation 1 (blue solid line) is scaled by a factor of 2.13 from the stress perturbation derived from the strong motion data at station 11628 for the Landers earthquake. Perturbation 2 (red solid line) is the same time series scaled up by a factor of 1.30. (b) Modeled surface fault slip velocity V_s (log scale) for the two cases. V_0 is the geological slip rate of SHF at 5 mm/yr. (c) Modeled surface slip resulting from the two perturbations. Horizontal dashed line in (a) shows triggering threshold at 0.75 MPa, and in (b) shows slip velocity V_s at 4 mm/s. Vertical dashed lines are plotted to help identify the phase alignment of noticeable triggered slip.

439

The time-integrated dynamic Coulomb stress perturbation also affects the triggering threshold and the displacement of triggered slip, in addition to the maximum Coulomb stress perturbation. In Figure 9, we show the results of three groups of simulations. Group

443   one is the original waveform for the Landers earthquake. In the other two groups, we

444   modify the original waveform by scaling both the normal and shear stress perturbations

445   by a factor of 0.5 (modified waveform 1, red) and 2 (modified waveform 2, black),

446   respectively, when the Coulomb stress change is negative (Figure 9a). This multiplication

447   factor artificially reduces or amplifies the negative Coulomb stress change but keeps the

448   positive Coulomb stress change the same for all the three groups. Then we scale each

449   group of perturbation by a common factor of 1.0-2.4 and apply them at timing of the

450   Landers earthquake. The scaling of triggered slip with maximum positive Coulomb

451   perturbation is different for the three groups of simulations (Figure 9b). Modified

452   waveform 1 requires less Coulomb stress to trigger 1 mm slip whereas modified

453   waveform 2 requires more (Figure 9d). The threshold scales linearly with the Coulomb

454   stress change integrated over the period of the wave train (Figure 9d). This shows that the

455   asymmetry of a waveform can also affect the ability to trigger fault creep, in addition to

456   just the maximum Coulomb stress change. The waveform with negative integrated

457   Coulomb stress change (black lines in Figure 9) can still trigger creep events mainly

458   because the nonlinear effect of stress perturbations on the slip velocity and state variable

459   (as shown in equations 1 and 2). To our knowledge, there is no previous study on the

460   asymmetry of waveforms for dynamic triggering.

461
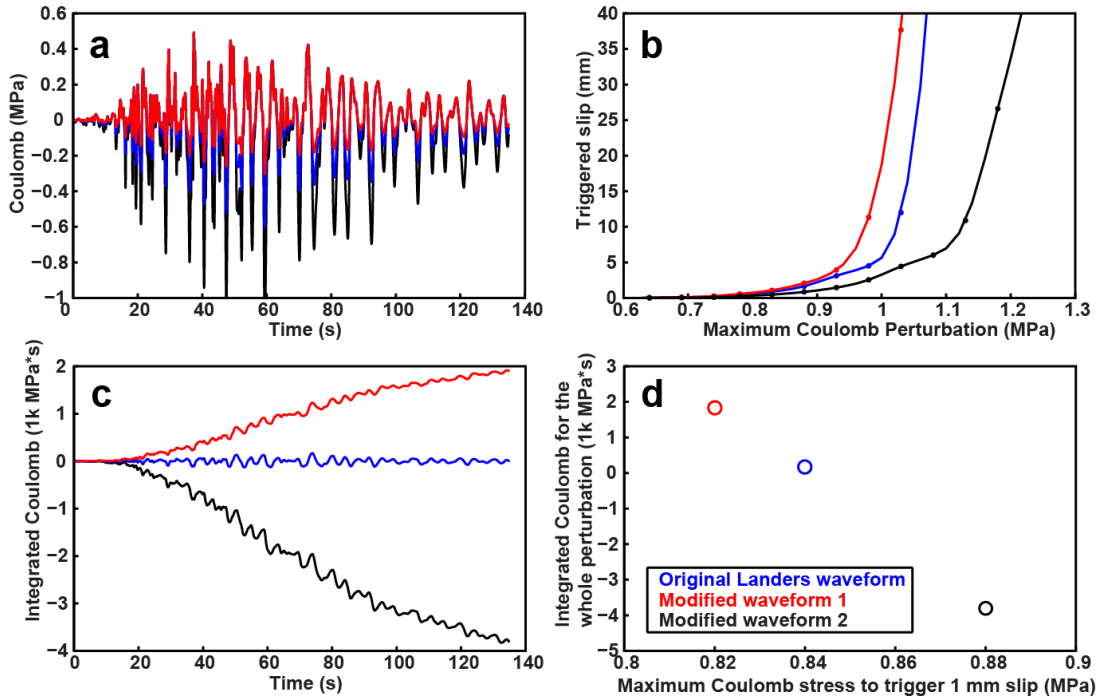
Figure 9. Effects of perturbations with asymmetric waveforms. (a) Reference perturbations of the three groups of simulations. For each group, we simulated the triggering by perturbations with the same waveform but scaled by different factors ranging from 1.0 to 2.4. (b) Triggered slip versus the maximum Coulomb stress change for the three groups of perturbations (c) Time-integrated Coulomb stress change for the three reference perturbations shown in (a). (d) Coulomb stress change integrated over the period of the wave train of the three reference perturbations scales linearly with the maximum Coulomb stress change needed to trigger 1 mm slip.

Discussion

Perfettini et al. (2003 a,b) studied static and dynamic triggering of earthquakes in a 1D fault model in the rate-and-state friction framework. They showed many characteristics that we have seen in our simulations including the instantaneous triggering of slip events. However, in Perfettini et al. (2003b), the instantaneous dynamic triggering threshold is about 7 MPa, whereas ours is an order of magnitude smaller at about 0.6 MPa for 0.01

476   mm slip and 0.8 MPa for 1 mm slip. This difference likely results from the different

477   parameters used for the fault segments that nucleate the slip events (Table S2 in the

478   supplementary material). The ratio of these thresholds (~11.7) is close to the ratio of the

479   nucleation sizes in the two studies (~10; 9 km versus 0.9 km) but not to that of normal

480   stress (~5) or Dc (~40). However, we find that the triggering threshold does not linearly

481   scale with the nucleation size. We consider three additional scenarios by decreasing (i)

482   the effective normal stress by 50% in the top 1 km, (ii) the Dc by 50% in the top 1 km,

483   and (iii) both the effective normal stress and Dc by 50% (and hence retaining the same

484   h^*) (Figure S3 in the supplementary material), where h^* is the nucleation size (Rubin and

485   Ampuero, 2005). The triggering threshold for 1 mm slip decreased from 0.84 to 0.75,

486   0.78, and 0.74 MPa for scenario (i), (ii), and (iii), respectively (Figure S3). Therefore,

487   the similar ratio between the triggering threshold and the nucleation size is a coincidence.

488   These results also suggest that the triggering threshold depends on the effective normal

489   stress and Dc even for the same h^*.

490

491   The dynamic Coulomb stress model has explained the asymmetry in aftershock

492   distribution of the 1992 Landers earthquake (Kilb et al., 2000), the instantaneously

493   triggering of earthquake in simulations by Perfettini et al. (2003b), and the

494   instantaneously triggering of creep events in our study. This is consistent with what

495   Parsons et al. (2014) have suggested that azimuth and polarization of surface waves

496   might be important for dynamic triggering of earthquakes. The polarization describes the

497   effect when seismic surface waves travel through heterogeneous structure, the wave

498   packets get refracted laterally, away from the source-receiver great circle (Laske et al.,

499   1994), which is different from the polarity of body waves. Both azimuth and polarization

500   of surface waves affect the dynamic Coulomb stress because perturbations caused by

501   surface waves need to be projected to the normal and shear direction of the fault.

502   Therefore, the same surface wave but different azimuth or polarization will cause

503   different dynamic Coulomb stress and triggered slip.

504

505   The findings we present in this paper are specific for the SHF site for a specific type of

506   fault slip. It is not yet clear how applicable our results are for other regions. For example,

507   creepmeters in Central California recorded many apparent fault-slip steps at times of

508   moderate local earthquakes of magnitudes 4–5 (King et al., 1977). It is possible to

509   conduct a similar study focusing on Central California. Moreover, the threshold of 0.6

510   MPa for dynamic triggering for creep events in Salton Trough seems larger than that for

511   triggering earthquakes in geothermal fields, 5 kPa (Brodsky and Prejean, 2005) and non-

512   volcanic tremors in subduction zones, 40 kPa in Cascadia (Rubinstein et al., 2007) and 60

513   kPa in Taiwan (Peng and Chao, 2008), non-volcanic tremors on San Andreas Fault, 2-3

514   kPa (Peng et al., 2009), and earthquakes near shale gas production sites in western

515   Alberta, Canada, 0.2-0.4 kPa (Wang et al., 2015). Many remotely triggered earthquakes

516   and non-volcanic tremors are believed to occur at locations with elevated pore pressure

517   and low effective normal stress of a few MPa (Hill et al., 1993; Brodsky and Prejean,

518   2005; Rubinstein et al., 2007). In contrast, the average normal stress change at the

519   shallow VW layer in our system is much larger at about 10 MPa. Moreover, the different

520   density of source population might also explain the different triggering threshold. As

521   shown in Perfettini et al. (2003b), dynamic triggering threshold drops dramatically if the

522   fault is very close to failure (<5% of interval), i.e. critically stressed. For a given study

523   region, there are much more tremor/earthquake (in geothermal fields) sources that are

524   very close to failure than creep-event sources and hence the observed triggering threshold

525   is much smaller for tremor/earthquake. All in all, if rate-and-state friction is the sole

526   mechanism that dictates triggering, the difference between triggering and non-triggering

527   should depend on the magnitude of the effective normal stress, the frictional properties,

528   or the density of source population of the system.

529

530   One key aspect of dynamic triggering as applied to earthquakes and tremor has been the

531   uncertainty in the physical mechanism that would cause the observed delays between the

532   applied stress perturbation and the occurrence of earthquake/tremor event. Shelly et al.

533   (2011) proposed that dynamic triggering of aseismic creep is a likely explanation for the

534   prolonged, dynamically triggered tremor sequences on the deep San Andreas Fault, and

535   by extension for many other delayed triggering earthquake or tremor sequences. Owing

536   to the source depth (~20 km) and small magnitude, those postulated creep events were

537   not detectable with geodetic data and instead inferred based on tremor migration rates

538   (10s of km/h) that are somewhat similar to creep event rupture velocities observed

539   elsewhere. A similar connection is observed in earthquake swarms in the Salton Trough

540   (Lohman and McGuire, 2007; Roland and McGuire, 2009). While the spontaneous creep

541   events on the SHF are not typically associated with any seismicity (Wei et al., 2011), they

542   do propagate at velocities (~100 km/hour; Bilham, 1989) similar to that inferred from the

543   tremor migration on the SAF (Shelly et al., 2011). On one hand, this suggests similar

544   frictional properties and stress conditions (Rubin, 2008; Roland and McGuire, 2009)

545   between 20 km depth at Parkfield and top 1 km in Salton Trough. On the other hand, this

546   seems contradictory to our suggestion that effective normal stress can explain the

547   different triggering threshold of tremor at 2-3 kPa (Peng et al., 2009) and creep events at

548   0.6 MPa (this study).

549

550   To look for the connection postulated by Shelly et al. (2011) we examined the

551   seismograms at a nearby seismic station (ERR of the Caltech Regional Seismic Network)

552   during the passing surface waves from the 2004 Mw 9.1 Sumatra, 2010 Mw 8.8 Chile,

553   2011 Mw 9.0 Tohoku, and 2012 Mw 8.6 Indian Ocean earthquakes which had maximum

554   velocities of 0.06, 0.11, 0.10, and 0.06 cm/s, respectively, but did not trigger any

555   detectable slip on the creepmeter or InSAR data. The corresponding stress perturbations

556   are about 5.1, 9.4, 8.6, and 5.1 kPa. Therefore, the lack of triggered creep is not

557   surprising because the normal stress of the shallow VW layer is quite high (~ 10 MPa)

558   and these ground motions are at least one order of magnitude smaller than that of the

559   1992 Landers, 1999 Hector Mine and 2010 El Mayor earthquakes.

560

561   Thus, while triggered creep is common on the SHF and other strike-slip faults in the

562   Salton Trough there is not a clear extrapolation of these events as a likely causative

563   source of prolonged tremor or earthquake sequences in other regions. In particular, the

564   observation that triggered creep events happen nearly instantaneously (Figure 6) in

565   contrast to multi-day spontaneous events suggests that triggered creep may have the same

566   difficulties explaining protracted sequences of triggered seismicity/tremor that last for

567   days following the transient dynamic stresses.

568

Conclusions

570   Not all creep events on the Superstition Hills fault are triggered by earthquakes, but of the

571   subset that accompany nearby earthquakes we show that dynamic stress changes during

572   the passage of seismic waves are most likely to have triggered slip. Numerical

573   simulations show that static stress changes from regional nearby large earthquakes

574   (M≥5.4) are typically less than 0.1 MPa and too small to instantaneously trigger creep

575   events, whereas dynamic perturbations alone are large enough to do so. The

576   instantaneous triggering of creep events depends on the peak amplitude of the Coulomb

577   stress change and the time-integrated dynamic Coulomb stress change. Observations

578   show that triggering of creep events on the Superstition Hills fault accompanies Mw>7

579   earthquakes within 150 km, Mw>6 earthquakes within 80 km, and Mw>5 earthquakes

580   within 20 km. Based on observations and simulations, the stress change amplitude

581   required to trigger a creep event of 0.01 mm surface slip is about 0.6 MPa. This is at least

582   one magnitude larger than the triggering threshold of non-volcanic tremor (2-60 KPa) and

583   earthquakes in geothermal fields (5 KPa) and near shale gas production sites (0.2-0.4

584   kPa), which may be due to the difference in effective normal stress, friction, or density of

585   source population in these systems or different triggering mechanisms. We conclude that

586   shallow frictional heterogeneity can explain both the spontaneous and dynamically

587   triggered creep events in our study area.

588

593

594 **References**

595 Allen, C. R., Wyss, M., Brune, J. N., Granz, A., and Wallace, R., 1972. Displacements on

596   the Imperial, Superstition Hills, and San Andreas faults triggered by the Borrego

597   Mountain Earthquake, in The Borrego Mountain Earthquake. U.S. Geol. Surv.

598   Prof. Pap. 787, 87–104.

599 Bilham, R., 1989. Surface slip subsequent to the 24 November 1987 Superstition Hills,

600   California, earthquake monitored by digital creepmeters. Bull. Seismol. Soc.

601   Am. 79, 424-450.

602 Bilham, R., Suszek, N., and Pinkney, S., 2004. California Creepmeters. Seismol. Res.

603   Lett. 75, 481-492, doi: 10.1785/gssrl.75.4.481.

604 Bock, Y., Melgar, D., and Crowell, B. W., 2011. Real-Time Strong-Motion Broadband

605   Displacements from Collocated GPS and Accelerometers. Bull. Seismol. Soc.

606   Am. 101, 2904-2925, doi: 10.1785/0120110007.

607 Bodin, P., Bilham, R., Behr, J., Gomberg, J. S., and Hudnut, K. W., 1994. Slip triggered

608   on Southern California faults by the 1992 Joshua Tree, Landers, and Big Bear

609   earthquakes. Bull. Seismol. Soc. Am. 84, 806–816.

610 Boore, D. M., and Bommer, J. J., 2005. Processing of strong-motion accelerograms:

611   Needs, options and consequences. Soil Dyn. Earth. Eng. 25, 93-115.

612   Brodsky, E., and Prejean, S. G., 2005. New constraints on mechanisms of remotely

613   triggered seismicity at Long Valley Caldera. J. Geophys. Res. 110, 1-14,

614   doi:10.1029/2004JB003211.

615   Cotton, F., and Coutant, O., 1997. Dynamic stress variations due to shear faults in plane-

616   layered medium. Geophys. J. Int. 128, 676–688.

617   Dieterich, J. H., 1979. Modeling of rock friction 1. Experimental results and constitutive

618   equations. J. Geophys. Res. 84, 2161–2168.

619   Du, W., Sykes, L. R., Shaw, B. E., and Scholz, C. H., 2003. Triggered aseismic fault slip

620   from nearby earthquakes, static or dynamic effect? J. Geophys. Res. 108, 1-21,

621   doi:10.1029/2002JB002008.

622   Fialko, Y., Sandwell, D., Agnew, D., Simons, M., Shearer, P., and Minster, B., 2002.

623   Deformation on nearby faults induced by the 1999 Hector Mine earthquake.

624   Science 297, 1858–1862.

625   Freed, A. M., 2005. Earthquake triggering by static, dynamic, and postseismic stress

626   transfer.   Annu.   Rev.   Earth   Planet.   Sci.   33,   335–367,

627   doi:10.1146/annurev.earth.33.092203.122505.

628   Gomberg, J., Beeler, N. M., Blanpied, M. L., and Bodin, P., 1998. Earthquake triggering

629   by transient and static deformations. J. Geophys. Res. 103, 24411–24426,

630   doi:10.1029/98JB01125.

631   Hauksson, E., Stock, J., Bilham, R., Boese, M., Chen, X., Fielding, E. J., Galetzka, J.,

632   Hudnut, K. W., Hutton, K., Jones, L. M., Kanamori, H., Shearer, P. M., Steidl, J.,

633   Treiman, J., Wei, S., and Yang, W., 2013. Report on the August 2012 Brawley

634   earthquake swarm in Imperial Valley, Southern California. Seismol. Res. Lett.

635   84, 177-189, doi: 10.1785/0220120169.

636 Hill, D. P., Reasenberg, P. A., Michael, A., Arabaz, W. J., Beroza, G., Brumbaugh, D.,

637   Brune, J. N., Castro, R., et al., 1993. Seismicity remotely triggered by the

638   magnitude 7.3 Landers, California, earthquake. Science 260, 1617.

639 Johnson, P., Savage, H., Knuth, M., Gomberg, J., and Marone, C., 2008. The effect of

640   acoustic waves on stick-slip behavior in sheared granular media: implications for

641   earthquake recurrence and triggering. Nature 451, 57-60

642   doi:10.1038/nature06440.

643 Kaneko, Y., and Lapusta, N., 2008. Variability of earthquake nucleation in continuum

644   models of rate-and-state faults and implications for aftershock rates. J. Geophys.

645   Res. 113, B12312, doi:10.1029/2007JB005154.

646 Kilb, D., Gomberg, J., and Bodin, P., 2000. Triggering of earthquake aftershocks by

647   dynamic stresses. Nature 408, 570-574.

648 King, G. C. P., Stein, R. S., and Lin, J., 1994. Static stress changes and the triggering of

649   earthquakes. Bull. Seismol. Soc. Am. 84, 935–953.

650 King, C.-Y., Nason, R. D., and Burford, R. O., 1977. Coseismic steps recorded on creep

651   meters along the San Andreas Fault. J. Geophys. Res. 82, 1655–1662,

652   doi:10.1029/JB082i011p01655.

653 Laske, G., Masters, G., and Zürn, W., 1994. Frequency-dependent polarization

654   measurements of long-period surface waves and their implications for global

655   phase velocity maps. Phys. Earth Planet. Int. 84, 111-137.

656   Lienkaemper, J. J., Galehouse, J. S., and Simpson, R. W., 2001. Long-term monitoring of

657   creep rate along the Hayward fault and evidence for a lasting creep response to

658   1989 Loma Prieta earthquake. Geophys. Res. Lett., 28, 2265-2268.

659   Linker, M. F., and Dieterich, J. H., 1992. Effects of variable normal stress on rock

660   friction: Observations and constitutive-equations. J. Geophys. Res. 97, 4923–

661   4940.

662   Liu, Y., 2013. Numerical simulations on megathrust rupture stabilized under strong

663   dilatancy strengthening in slow slip region. Geophys. Res. Lett. 40, 1311-1316,

664   doi:10.1002/grl.50298.

665   Lohman, R. B., and McGuire, J. J., 2007. Earthquake swarms driven by aseismic creep in

666   the Salton Trough, California. J. Geophys. Res. 112, doi:B04405

667   10.1029/2006jb004596.

668   Louie, J. N., Allen, C. R., Johnson, D. C, Haase, P. C., and Cohn, S. N., 1985. Fault slip

669   in southern California. Bull. Seismol. Soc. Am. 75, 811–833.

670   McGuire, J. J., Lohman, R. B., Catchings, R. D., Rymer, M. J., and Goldman, M. R.,

671   2015. Relationships among seismic velocity, metamorphism, and seismic and

672   aseismic fault slip in the Salton Sea Geothermal Field region. J. Geophys. Res.

673   120, 2600–2615, doi: 10.1002/2014JB011579.

674   Parsons, T., Segou, M., and Marzocchi, W., 2014. Invited Review: The global aftershock

675   zone. Tectonophysics 618, 1-34, doi: 10.1016/j.tecto.2014.01.038.

676   Peng, Z., and Chao, K., 2008. Non-volcanic tremor beneath the Central Range in Taiwan

677   triggered by the 2001 M w 7.8 Kunlun earthquake. Geophys. J. Int. 175, 825–

678   829, doi:10.1111/j.1365-246X.2008.03886.x.

679   Peng, Z., Vidale, J. E., Wech, A. G., Nadeau, R. M., and Creager, K. C., 2009. Remote

680   triggering of tremor along the San Andreas Fault in central California. J.

681   Geophys. Res. 114, 1–18, doi:10.1029/2008JB006049.

682   Perfettini, H., Schmittbuhl, J., and Cochard, A., 2003a. Shear and normal load

683   perturbations on a two-dimensional continuous fault: 1. Static triggering. J.

684   Geophys. Res. 108, doi: 10.1029/2002JB001804.

685   Perfettini, H., Schmittbuhl, J., and Cochard, A., 2003b. Shear and normal load

686   perturbations on a two-dimensional continuous fault: 2. Dynamic triggering. J.

687   Geophys. Res. 108, doi: 10.1029/2002JB001805.

688   Richards-Dinger, K., Stein, R. S., and Toda, S., 2010. Decay of aftershock density with

689   distance does not indicate triggering by dynamic stress. Nature 467, 583-586,

690   doi:10.1038/nature0940.

691   Richardson, E., and Marone, C. J., 1999. Effects of normal stress vibrations on frictional

692   healing. J. Geophys. Res. 104, 28,859–28,878.

693   Roland, E., and McGuire, J. J., 2009. Earthquake swarms on transform faults. Geophys. J.

694   Int. 178, 1677-1690.

695   Rubin, A. M., 2008. Episodic slow slip events and rate-and-state friction. J. Geophys.

696   Res. 113, doi:10.1029/2008jb005642.

697   Rubin, A. M., and Ampuero, J. P., 2005. Earthquake nucleation on (aging) rate-and-state

698   faults. J. Geophys. Res. 110, B11312.

699   Rubinstein, J. L., Vidale, J. E., Gomberg, J., Bodin, P., Creager, K. C., and Malone, S. D.,

700   2007. Non-volcanic tremor driven by large transient shear stresses. Nature 448,

701   579-582, doi: 10.1038/nature06017.

702 Ruina, A. L., 1983. Slip instability and state variable friction laws. J. Geophys. Res. 88,

703   10,359– 10,370.

704 Rymer, M. J., Boatwright, J., Seekins, L. C., Douglas Yule, J., and Liu, J., 2002.

705   Triggered Surface Slips in the Salton Trough Associated with the 1999 Hector

706   Mine, California, Earthquake. Bull. Seism. Soc. Am. 92, 1300-1317,

707   doi:10.1785/0120000935.

708 Scholz, C., 1998. Earthquakes and friction laws. Nature 391, 37-42, doi:10.1038/34097.

709 Schulz, S., Burford, R. O., and Mavko, B., 1983. Influence of Seismicity and Rainfall on

710   Episodic Creep on the San Andreas Fault System in Central California. J.

711   Geophys. Res. 88, 7475-7484.

712 Segall, P., Rubin, A. M., Bradley, A. M., and Rice, J. R., 2010. Dilatant strengthening as

713   a mechanism for slow slip events. J. Geophys. Res. 115, B12305,

714   doi:10.1029/2010JB007449.

715 Shelly, D. R., Peng, Z., Hill, D. P., and Aiken, C., 2011. Triggered creep as a possible

716   mechanism for delayed dynamic triggering of tremor and earthquakes, Nature

717   Geosci. 4, 384-388,

718 Simpson, R. W., Schulz, S. S., Dietz, L. D., and Burford, R. O., 1988. The response of

719   creeping parts of the San Andreas fault to earthquakes on nearby faults: Two

720   examples. Pure Appl. Geophys. 126, 665–685.

721 Stein, R. S., 1999. The role of stress transfer in earthquake occurrence. Nature 402, 605-

722   609, doi:10.1038/45144.

723 Wang, B., Harrington, R. M., Liu, Y., Yu, H., Carey, A., and van der Elst, N. J., 2015.

724   Isolated cases of remote dynamic triggering in Canada detected using cataloged

725   earthquakes combined with a matched-filter approach. Geophys. Res. Lett. 42,

726   DOI: 10.1002/2015GL064377.

727   Wei, M., Sandwell, D., Fialko, Y., and Bilham, R., 2011. Slip on faults in the Imperial

728   Valley triggered by the 4 April 2010 Mw 7.2 El Mayor-Cucapah earthquake

729   revealed   by   InSAR.   Geophys.   Res.   Lett.   38,   L01308,

730   doi:10.1029/2010GL045235.

731   Wei, M., Kaneko, Y., Liu, Y., and McGuire, J. J., 2013. Episodic fault creep events in

732   California controlled by shallow frictional heterogeneity. Nature Geosci. 6, 1–5,

733   doi:10.1038/ngeo1835.

734   Williams, P., and Magistrale, H. W., 1989. Slip on the Superstition Hills fault

735   associated with the 24 November 1987 Superstition Hills, California,

736   earthquake. Bull. Seism. Soc. Am. 79, 390-410.

737

Supplementary materials

740

741 **Table S1. Significant earthquakes (M ≥ 5.4) within 200 km of the Salton Trough.**

742 The left column under each fault indicates if triggered slip occurred or if there were an

743 earthquake on the fault: Y: triggered slip observed; N: no triggered slip; O: mainshock on

744 the fault. The right column shows the distance (km) between the earthquake epicenter and

745 the center of the fault.

| Year	Mw	Earthquake	SAF Triggering		SHF Triggering		Imperial Triggering		Coyote Creek Triggering	
1951	5.95	30 km west of Mexicali, Mexico	N/A	120	Y	68	N/A	35	N/A	100
1954	6.4	Arroyo Salada	N/A	30	Y	50	N/A	80	N/A	25
1968	6.5	Borrego Mountain	Y	40	Y	40	Y	75	O	O
1979	6.4	Imperial	Y	100	Y	45	O	O	Y	75
1980	6.3	Victoria, Mexico	N/A	160	N/A	100	N/A	70	N/A	125
1981	5.75	Westmorland	N	50	Y	20	Y	35	N	40
1986	6.0	North Palm Springs	Y	88	N	139	N	170	N	119
1987	6.6/6.2	Superstition Hills/Elmore Ranch	Y	55	O	O	Y	40	Y	20
1992	6.1/7.3/6.3	Joshua Tree/Landers/Big Bear	Y	90	Y	155	N	175	N	140
1999	7.1	Hector Mine	Y	130	Y	190	Y	205	N	175
2002	5.7	Near El Mayor, Mexico	N/A	135	N/A	80	N/A	50	N/A	110
2009	5.8	Near El Mayor, Mexico	N/A	130	N/A	70	N/A	40	N/A	105
2010	7.2	El Mayor-Cucapha, Mexico	Y	145	Y	85	Y	65	Y	105
2012	5.4	Brawley	N/A	60	Y	15	N/A	25	N/A	45

746

747

748

749 **Table S2: Comparison of model parameters between Perfettini et al., 2003a,b**
750 **and this paper.**
751

Parameters	Perfettini et al. (2003a,b)	This study
Dc (mm)	20	0.2-0.7
a-b (a)	-0.004 (0.015)	-0.004 (0.015)
Normal stress (MPa)	50	5.6 – 15.6
Shear modulus (GPa)	30	30
Nucleation size (km)*	9	0.9
Threshold for dynamic triggering (MPa)	9-10	0.6

752

753 * Nucleation size $h^* = \frac{2\mu b D_c}{\pi(b-a)^2 \overline{\sigma}}$ (Rubin and Ampuero, 2005)

754
755
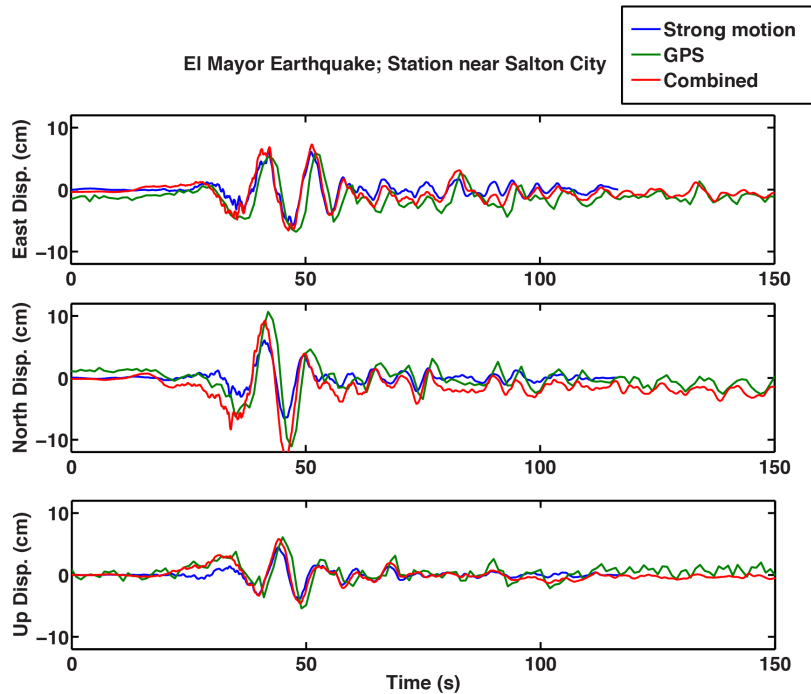
756
757 **Figure S1.** Comparison between strong motion and high-rate GPS measurements at station 11628

758 near Salton City. The time series combines both strong-motion and GPS data and provides the

759 best estimate of ground motion (Bock et al. 2001). High-rate GPS and "Combined" records are

760 from Bock et al. (2011).
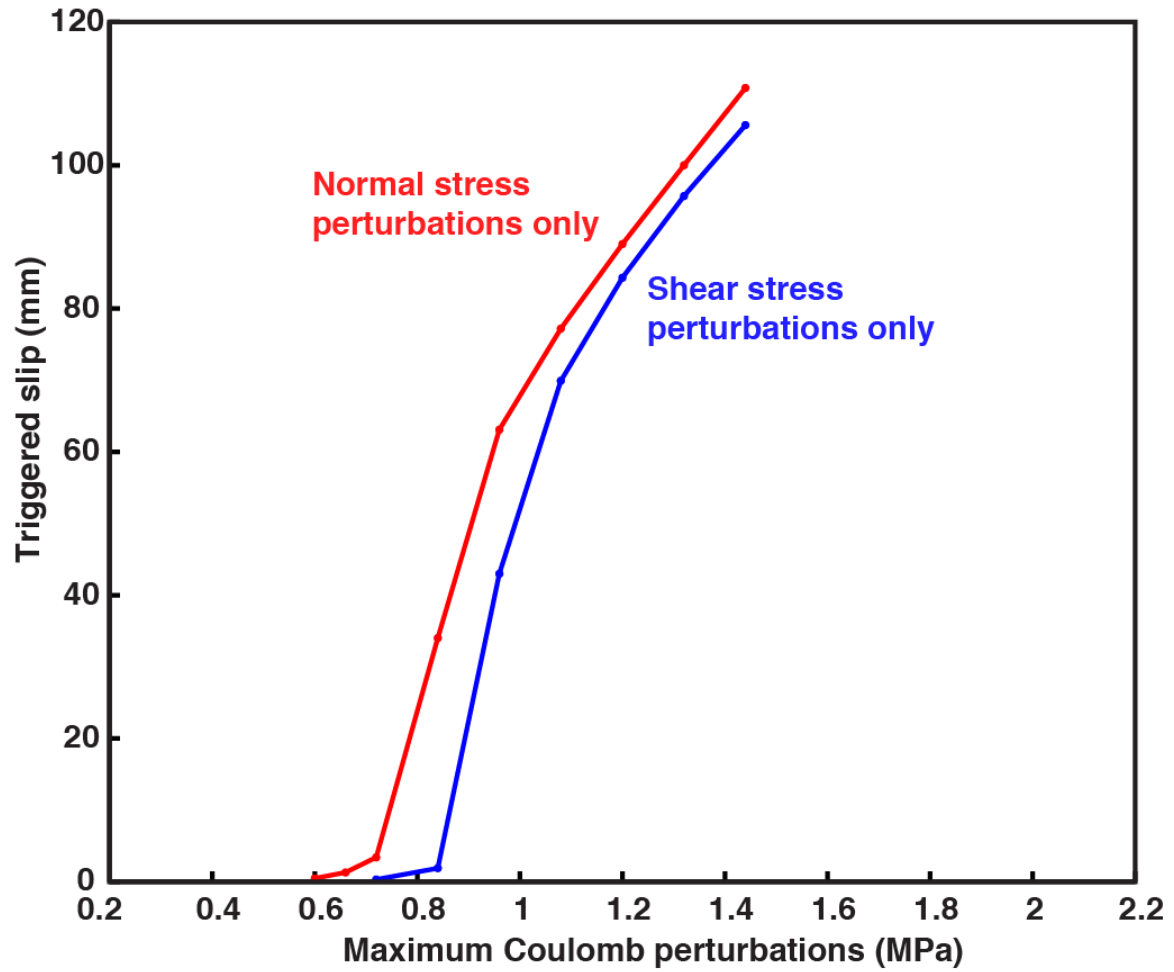
761
762
763 **Figure S2.** Simulation results of triggered slip produced by pulse perturbations for shear stress

764 perturbations only (blue) and normal stress perturbation only (red). This shows that the

765 maximum Coulomb stress change is a good indicator for triggered slip.

766

767

768
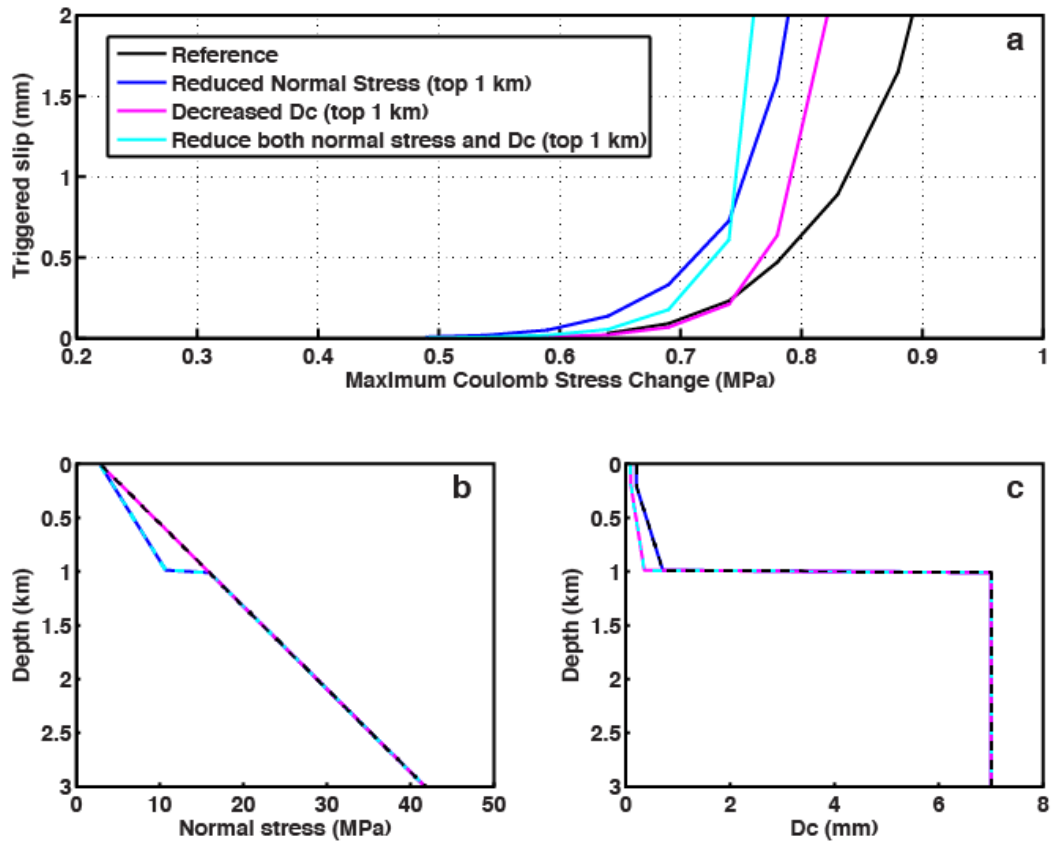
Figure S3. Simulations of triggered slip for the reference model and models with reduced effective normal stress, *Dc,* and both stress and *Dc*. Black, blue, magenta, and cyan solid lines represent the simulation results and parameters for the reference model, the reduced normal stress model, and the reduced *Dc* model, and the reduced stress and *Dc* model respectively. All groups of simulations used the perturbations based on the Landers waveform at the same time of perturbation. (a) Triggered slip versus maximum dynamic Coulomb stress change for the three simulations. (b) Effective normal stress used in the simulations. The effective normal stress is the same for the reference and reduced Dc simulations. (c) *Dc* used, same for the reference and reduced normal stress simulations.